



Contents lists available at ScienceDirect

# International Journal of Applied Earth Observations and Geoinformation

journal homepage: [www.elsevier.com/locate/jag](http://www.elsevier.com/locate/jag)

## Multi-resolution topographic analysis in hexagonal Discrete Global Grid Systems

Mingke Li<sup>a,\*</sup>, Heather McGrath<sup>b</sup>, Emmanuel Stefanakis<sup>a</sup><sup>a</sup> Department of Geomatics Engineering, Schulich School of Engineering, University of Calgary, Calgary, Canada<sup>b</sup> Canada Centre of Mapping and Earth Observation, Natural Resources Canada, Ottawa, Canada

## ARTICLE INFO

## Keywords:

Discrete Global Grid Systems  
 Topographic analysis  
 Multi-resolution  
 Map algebra

## ABSTRACT

Discrete Global Grid Systems (DGGS) have been increasingly adopted as a standard framework for multi-source geospatial data. Previous research largely studied the mathematical foundation of discrete global grids, developed open-source libraries, and explored their application as data integration platforms. This study investigated the multi-resolution terrain analysis in a pure hexagonal DGGS environment, including descriptive statistics, topographic parameters, and topographic indices. Experiments across multiple grid resolutions were carried out in three study areas with different terrain roughness in Alberta, Canada. Five algorithms were proposed to calculate both the slope gradient and terrain aspect. A cell-based pair-wise comparison showed a strong positive correlation between the gradient values as calculated from five algorithms. The grid resolutions as well as the terrain roughness had a clear effect on the computed slope gradient and topographic indices. This research aims to enhance the analytical functionality of hexagonal DGGS to better support decision-making in real world problems.

### 1. Introduction

Geographic grid systems emerged as consistent structures to fulfill the needs of digitizing, modeling, and organizing heterogeneous geospatial elements in the real world (Foster et al., 2001). A geographic grid is used to abstract the geographic space into a mathematical space where algorithms, aggregations, and statistics can be applied, and a geographic grid system normally consists of a sequence of geographic grids with different granularities. Discrete Global Grid Systems (DGGS) are a standard of Earth reference grid systems, documented by the Open Geospatial Consortium (OGC) and International Organization for Standardization (ISO) 19170-1:2021 (ISO, 2021; OGC, 2017). DGGS offer a mathematical, hierarchical tessellation of the Earth's surface by almost identical cells without any overlaps or gaps, along with cell indices, and demonstrate benefits in modeling and analyzing geospatial data by their interoperability and parallel-computation potentials (Alderson et al., 2020; Mahdavi-Amiri et al., 2015).

One of the earliest studies on DGGS was the Geodesic Elevation Model (GEM) which was used to access, assemble, and encode point elevation data in a triangular global grid framework (Dutton, 1984). A simpler structure, the Quaternary Triangular Mesh (QTM), was

proposed later to support the needs of map generalization (Dutton, 1999). Examples of open-source DGGS libraries developed in recent years include the H3 (Uber, 2017), OpenEAGGR (OpenEAGGR, 2017), and DGGRID (wrapped as open-source libraries in other programming languages such as the dggridR library in R programming; Barnes and Sahr, 2017). DGGS are discrete and hierarchical, with a deterministic cell coverage of locations at a certain resolution. Thus, DGGS have been increasingly used as a standard framework to integrate heterogeneous spatial data in recent literature. For example, Li et al. (2021) used a DGGS to integrate multi-source terrain data and set the stage for a national elevation service in Canada. Maritime risk maps were created by machine learning algorithms using a DGGS as the data integration structure (Rawson et al., 2021). In addition, analytical operations in DGGS were investigated in a few studies. An integrated environmental analytics system was designed based on a DGGS and revealed its ability in dynamic environmental modeling, where operations such as map algebra, set operations, buffering, and network analysis were explored (Robertson et al., 2020). A QTM-based point data aggregation and rendering platform was developed and origin-destination flow visualization techniques were performed upon it (Raposo et al., 2019; Raposo, 2019). Crusta, a virtual globe was produced based on a 30-sided

\* Corresponding author at: Department of Geomatics Engineering, Schulich School of Engineering, University of Calgary, 2500 University Drive NW, Calgary, Alberta T2N 1N4, Canada.

E-mail addresses: [mingke.li@ucalgary.ca](mailto:mingke.li@ucalgary.ca) (M. Li), [heather.mcgrath@canada.ca](mailto:heather.mcgrath@canada.ca) (H. McGrath), [emmanuel.stefanakis@ucalgary.ca](mailto:emmanuel.stefanakis@ucalgary.ca) (E. Stefanakis).

<https://doi.org/10.1016/j.jag.2022.102985>

Received 7 March 2022; Received in revised form 17 June 2022; Accepted 14 August 2022

1569-8432/© 2022 Published by Elsevier B.V. This is an open access article under the CC BY-NC-ND license (<http://creativecommons.org/licenses/by-nc-nd/4.0/>).

polyhedron, providing the dynamic shading of terrain surface at an arbitrary desired resolution (Bernardin et al., 2011).

In this paper, we aimed to conduct multi-resolution terrain analysis in an Icosahedral Snyder Equal Area Aperture 3 Hexagonal Grid (ISEA3H) DGGs. Key advantages of the ISEA3H tessellation have been noted previously by comparing it to other DGGs configurations (Sahr et al., 2003; White et al., 1998). Particularly, in terms of the topographic analytics on terrain data, hexagonal cell geometry can eliminate the ambiguity of the cell neighborhood and weighting scheme of the focal spatial operations, such as the slope gradient computation, due to its uniform adjacency (Li et al., 2021). Aperture 3 means that the area ratio between a parent cell and a child cell at two successive levels is three. Compared to aperture 4 or aperture 7 hexagonal tessellation, aperture 3 guaranteed the monotone convergence regarding the point displacement, which means that a finer resolution resulted in less displacement between the original point location and the corresponding cell centroid location. Previous research examined the algorithms to compute hydrological geomorphometry parameters on regular grids other than rectangular ones. Wang et al. (2020) showed the process of extracting valley lines on hexagonal grids and compared the results to square grids, concluding that hexagonal grids had a greater ability to maintain the detailed shape and location accuracy, while having a weaker capability to extract valley lines among flat regions. A regular hierarchical surface model introduced by Wright (2017) generalized the hydrological parameter computation onto hexagonal and triangular grids, and incorporated a scaling function to form a pyramid framework.

We developed four categories of analytical functions (introduced in Section 2): 1) focal statistics, 2) zonal statistics, 3) topographic parameters including slope gradient and aspect, curvature, and hill-shade, and 4) topographic indices including Terrain Roughness Index (TRI) and Topographic Position Index (TPI). We also classified our developed operations by referring to Tomlin’s map algebra model and extending the architecture into the DGGs context, namely the operations on individual locations (i.e., local operations), operations within neighborhoods (i.e., focal operations), and operations within zones (i.e., zonal

operations; Tomlin, 1990). To provide a thorough reference for future DGGs functionality development, we examined five approaches to generate slope gradient and aspect in the ISEA3H DGGs environment. Experiments at multiple resolutions were carried out over three study areas with different levels of roughness in Alberta, Canada.

The remainder of this paper is arranged as follows. In Section 2, we introduce the detailed algorithms developed for various analytical functions. Section 3 provides the background of three study areas and the computational environment. Section 4 shows the experiment process and presents the experiment results. Section 5 discusses the research and points out the study impact. Section 6 concludes the paper.

## 2. Topographic operations in DGGs

Fig. 1 shows the local, focal, and zonal classifications of the developed operations in this study. The detailed algorithms are introduced below.

### 2.1. Focal statistics

Computing focal statistics was one of the focal operations developed in this research, where neighbor navigation was the first step of all focal analytics (Fig. 1). In the ISEA3H DGGs, neighbors of a target cell at a certain level can be determined according to a coordinate-based cell indexing mechanism (Mahdavi-Amiri et al., 2015). Typically, Quadrilateral 2-Dimensional Integer (Q2DI) indexing has been implemented in the DGGRID library and its R interface dggridR, which firstly partitions the Earth’s surface into 12 quad tiles, as shown in Fig. 2, and provides the (i, j) coordinate on the certain quad for each cell at each level (Barnes and Sahr, 2017). In the ISEA3H DGGs, there is a relative 30° shift of the hexagonal grids’ orientation, hence the hexagonal grids’ coordinate axes, between every two successive resolutions (Sahr, 2008). Sahr (2008) managed to standardize the coordinate axes among different resolutions and simplify the indexing method in the ISEA3H tessellation by assigning the coordinate of a cell at an odd-resolution level the

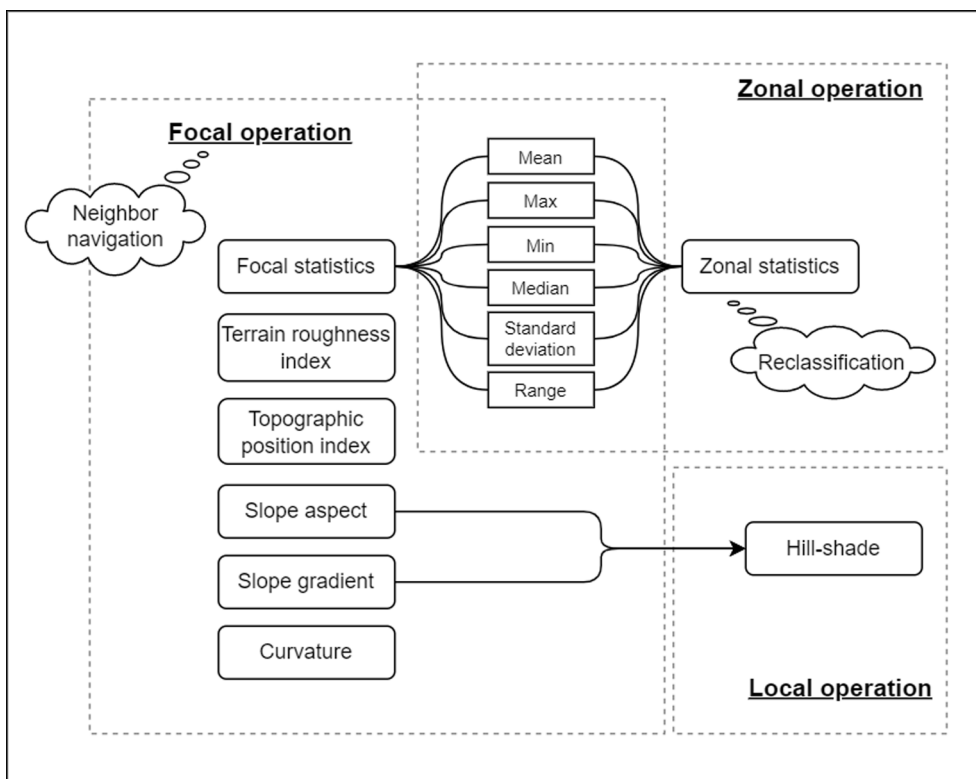


Fig. 1. Classification of the developed operations in this study.

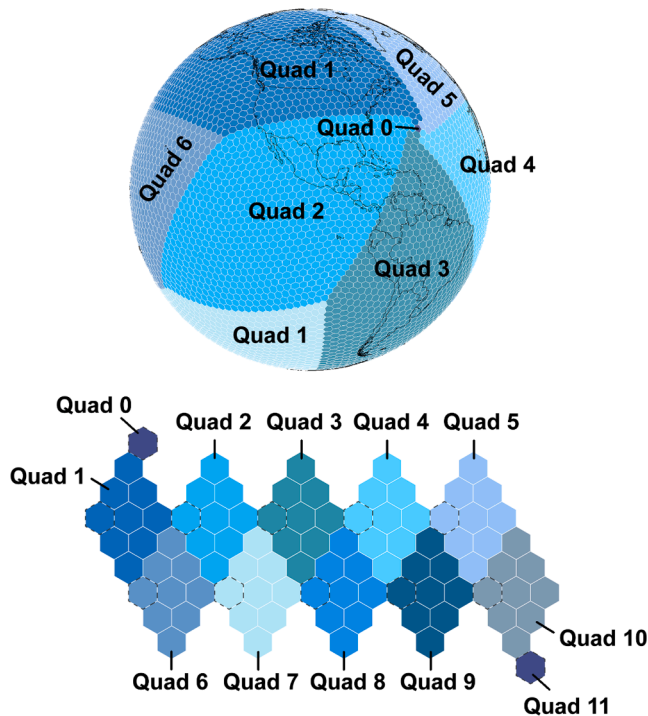
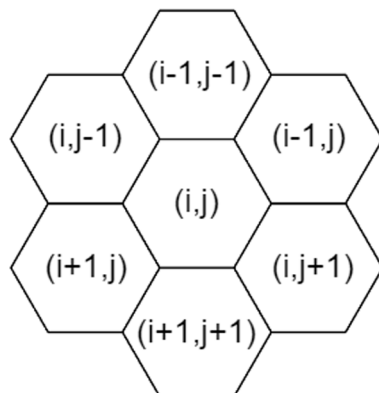


Fig. 2. The spherical and unfolded quad tile structure of the ISEA3H DGGs with the Q2DI indexing. Twelve pentagons are shown as hexagons in the unfolded quad tiles. (For interpretation of the references to colour in this figure legend, the reader is referred to the web version of this article.)

coordinate of the centroid-aligned cell at the consecutive finer even-resolution level. Depending on the Q2DI indexing mechanism, the  $(i, j)$  coordinates of six neighbors of each of the cells on the same quad can be found based on the center cell's coordinate. For example, Fig. 3 shows the coordinates of six neighbors of the center cell in the first quad at even- and odd-resolution levels. In this study, the size of the neighborhood was defined by the number of rings of hexagonal cells, and the extended neighborhood was determined recursively by adding the outer ring to the inner rings (Fig. 4). When an area of interest is larger than one quad, focal operations need cross-quad neighbor navigation considering the quad numbers as well as the cell coordinates. In this study, we focused on the scenarios where all target cells and their neighbors were on the same quad.

Given the determined neighborhood, the focal statistical algorithm is

**a. Even-resolution level**



**b. Odd-resolution level**

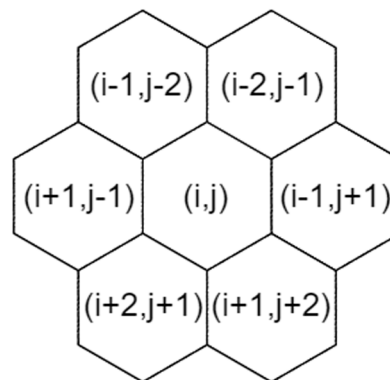


Fig. 3. Quadrilateral 2-Dimensional Integer (Q2DI) coordinates of six neighboring cells of each center cell at an a. even-resolution level and b. odd-resolution level in the first quad.

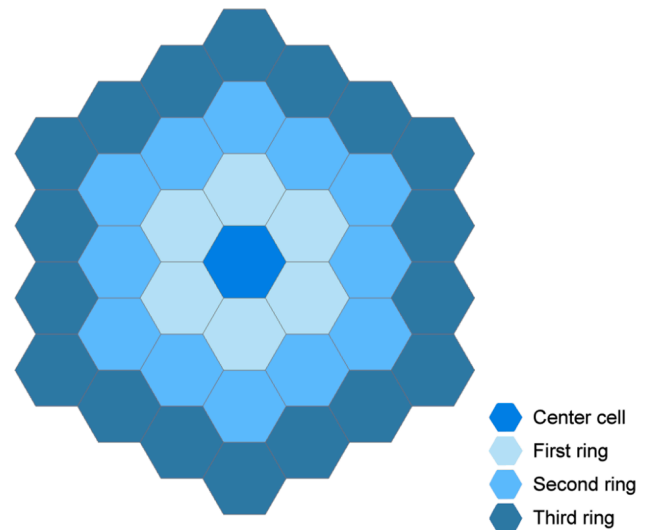


Fig. 4. Illustration of the neighborhood around a center cell defined by the number of rings. (For interpretation of the references to colour in this figure legend, the reader is referred to the web version of this article.)

then used to calculate descriptive statistics among the neighboring cells and assign the computed values to the center cell at the same DGGs resolution level. Basically, the focal statistics are straightforward, which use neighboring cells' indices as keys to extract elevation values accordingly and compute statistics. In this study, mean, maximum, minimum, median, standard deviation, and range were computed (Fig. 1). Edge cells without a complete neighborhood are assigned null values for all focal statistics.

**2.2. Zonal statistics**

Zonal statistics are zonal operations that start from reclassifying cells according to the defined zones, for example, forest stands. The reclassification process in DGGs depends on the original data model that provides spatial information on zones of interest. For instance, if the zone information is in raster format with discrete, numeric values representing nominal zones, the reclassification will essentially be a quantization process using the nearest neighbour interpolation. In the case of vector format, the reclassification process will be analogous to a vector-to-raster conversion, namely a rasterization process. This can be done following the largest-share principle, where the cell received the

zone attribute which covers the majority of its area, or the central-point principle, which assigns the zone identities to a cell if the cell centroid spatially falls in a certain zone (Shortridge, 2004). The reclassification process can also employ other more sophisticated approaches such as considering a Gaussian point spread function around the centroid (Zhang et al., 2007). In our implementation, we adopted the central-point principle for vector zone data and used the nearest neighbor resampling for raster zone data. After reclassifying cells and determining cell identities, zonal statistics are to calculate the mean, maximum, minimum, median, standard deviation, and range grouped by the zone identities, and to assign the values to all DGGs cells belonging to each of the zones based on the indexing system (Fig. 1).

2.3. Topographic parameters

2.3.1. Slope gradient and aspect

According to Burrough and McDonell (1998), the slope of a surface has two components: gradient and aspect. Computing slope gradient and aspect is considered as a focal operation. From the perspective of geography, the slope gradient is the maximum rate of change in altitude with regard to the horizontal plane, and the slope aspect is the compass direction toward which the inclined surface has the steepest descent (Tomlin, 1990). From the perspective of 2D signal processing, slope gradient and aspect are essentially the first derivatives of the 2D signal, i.e., the surface (Amatulli et al., 2020). From the perspective of mathematical geometry, in a 3D Cartesian coordinate system, the slope gradient and aspect can be computed from the normal vector of a local plane surface, where the gradient is the angle between the normal line and the vertical axis, and the aspect equals to the angle between true north and the projection of the normal line on the horizontal surface

(Hodgson, 1998; Wright, 2017).

In our research, flat areas, i.e., target cells sharing the common elevations as all their neighboring cells, received 0 for the slope gradient and  $-1$  for the slope aspect, where  $-1$  represented null values. Edge cells that do not have a complete neighborhood received null values for both the slope gradient and aspect. Based on different perspectives of the slope definition, five approaches to calculating slope gradient and aspect were developed and tested (Fig. 5): Maximum Adjacent Gradient (MAG), Maximum Downward Gradient (MDG), Multiple Downhill Neighbors (MDN), Finite-Difference Algorithm (FDA), and Best-Fit Plane (BFP) methods (Hodgson, 1998; Shanholtz et al., 1990; Travis, 1975; Wolock and McCabe, 1995). These five approaches were derived from those algorithms used on traditional, rectangular terrain rasters, and were extended into the ISEA3H DGGs context.

The MAG method calculates the absolute maximum differences between the center cell and its neighbors (Shanholtz et al., 1990; Fig. 5). For the calculation on rectangular raster cells, ambiguity arises when defining the neighborhood, where one can account for four orthogonal neighbors or eight neighbors including another four diagonal neighbors. Nonetheless, in the hexagonal grids, cells are uniformly adjacent so that a neighborhood can be precisely defined. In our research, we only considered six neighbors, i.e., the first ring, for each cell when computing the topographic parameters (Fig. 4). The neighbors are scanned clock-wise from the north, and the neighbor with the maximum elevation difference is determined. Thus, the slope gradient is the absolute difference between the center cell and the determined cell normalized by their cell spacing. The aspect is the direction of the determined cell if the slope is downhill or the directly opposite direction if the slope is uphill (Skidmore, 1989).

The MDG method is similar to the MAG method, except that it

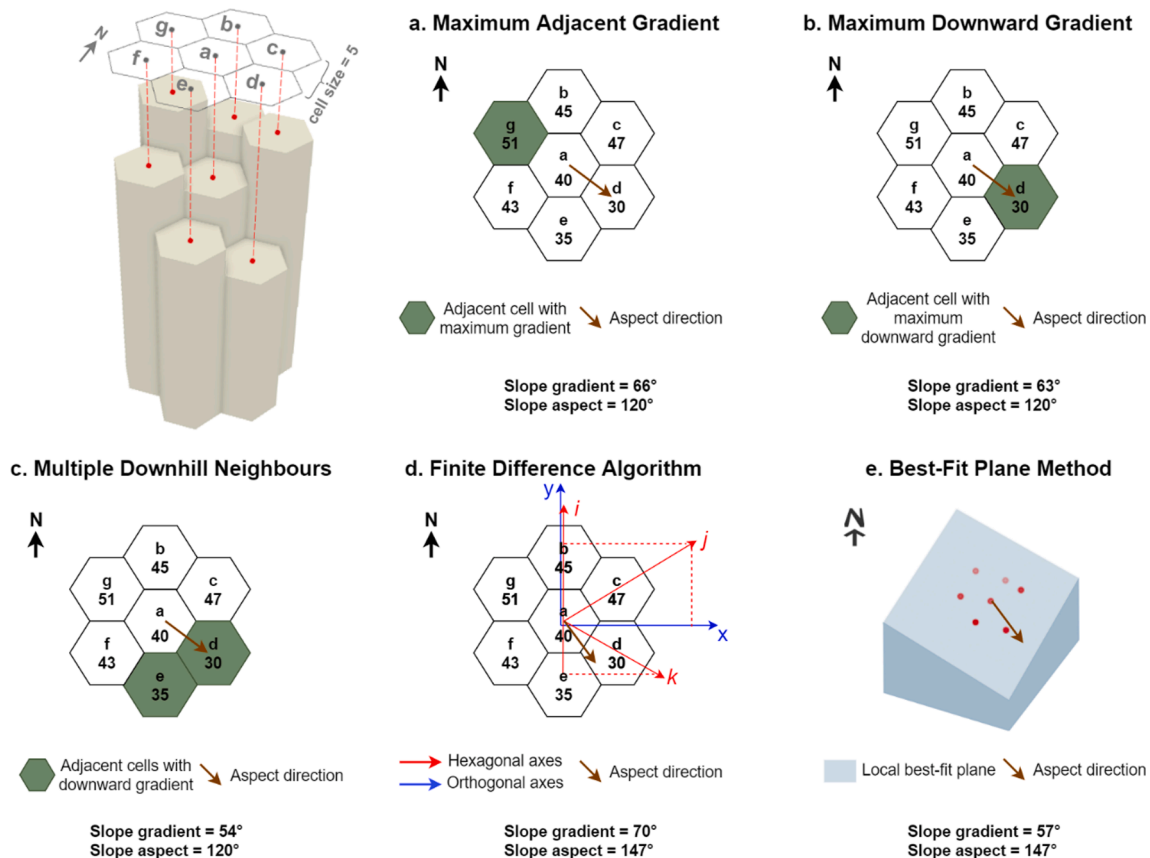


Fig. 5. Illustration of five methods to calculate slope gradient and aspect at even-resolution levels: a. Maximum Adjacent Gradient, b. Maximum Downward Gradient, c. Multiple Downhill Neighbors, d. Finite-Difference Algorithm, and e. Best-Fit Plane. (For interpretation of the references to colour in this figure legend, the reader is referred to the web version of this article.)

considers the maximum downward differences between the center cell and its neighbors (Travis, 1975; Fig. 5). This can help to preserve local variability without overestimating the slope gradient (Dunn and Hickey, 1998). Problems arise when the center cell does not have any neighbors with lower elevations, which is known as a depression. We treated depressions by ‘filling’ the cell to the lowest elevation in its neighbors so that the slope gradient received the value of 0 and the aspect is the direction to the lowest neighbor. In both cases of the MAG and MDG methods, the generated aspect is limited to six possible directions for each target cell. Because there is a 30° shift of the hexagonal grids’ orientation between every two successive resolutions in the ISEA3H DGGs, six possible directions of the aspect are 0°, 60°, 120°, 180°, 240°, and 300° on even-resolution levels, and 30°, 90°, 150°, 210°, 270°, and 330° on odd-resolution levels.

Different from the MDG method, all downward neighbors contribute to the slope calculation for each center cell when applying the MDN method (Wolock and McCabe, 1995; Fig. 5). Slope gradient is calculated as the arithmetic average of the elevation differences between the center cell and the downhill neighboring cells normalized by the cell spacing. Because the slope aspect is a circular-scale measurement, namely a periodic value from 0 to 360°, the average aspect cannot be simply viewed as the arithmetic average of all downhill neighbors’ direction angles. Therefore, a ‘mean vector’ was used to represent the orientation of the ‘mean surface’ (Hodgson, 1998). Specifically, separate triangular facets are composed by connecting the center cell’s centroid and the centroids of the downward neighbors, and the ‘mean vector’ is the sum of the normal vectors of these triangular facets. The slope aspect is then computed as the angle between the true north and the projection of this ‘mean vector’ on the horizontal surface (Hodgson and Gaile, 1996). Fig. 6 illustrates the computation of the slope aspect of a central cell with three downhill neighbors in its first-ring neighborhood. Two special situations need to be treated when applying the MDN method. First, if the center cell is a depression, the slope gradient will be 0 and the aspect will be the direction of the neighbor with the lowest elevation. Second, if two downhill neighboring cells are found and are in two opposite directions, then the slope gradient and aspect will be treated by the MDG method.

The FDA method calculates the finite difference of elevations over the hexagonal grid (Fig. 5). Elevation differences along three native axes

of hexagonal grids are projected to two orthogonal axes, and the final slope gradient and aspect are computed by combining these two orthogonal partial derivatives. The computation method is derived from the finite difference algorithm over rectangular grids, while hexagonal neighbors receive equal weight because of their uniform adjacency. The specific slope gradient and aspect in the hexagonal grid are adjusted from the calculation in rectangular grids, and are calculated as (Hodgson, 1998):

$$gradient = ATAN \left( \frac{\sqrt{(dx)^2 + (dy)^2}}{cell\ spacing} \right) \tag{1}$$

$$aspect = ATAN2(dy, -dx) \tag{2}$$

where on even-resolution levels, the elevation differences along two orthogonal axes y and x are

$$dy = di + dj \cdot \sin \frac{\pi}{6} - dk \cdot \sin \frac{\pi}{6} \tag{3}$$

$$dx = dj \cdot \cos \frac{\pi}{6} + dk \cdot \cos \frac{\pi}{6} \tag{4}$$

and on odd-resolution levels are.

$$dy = di \cdot \cos \frac{\pi}{6} + dj \cdot \cos \frac{\pi}{6} \tag{5}$$

$$dx = dk + dj \cdot \sin \frac{\pi}{6} - di \cdot \sin \frac{\pi}{6} \tag{6}$$

where the elevation differences along three hexagonal axes i, k, and j are.

$$di = \frac{(e - a) + (a - b)}{2} \tag{7}$$

$$dk = \frac{(g - a) + (a - d)}{2} \tag{8}$$

$$dj = \frac{(f - a) + (a - c)}{2} \tag{9}$$

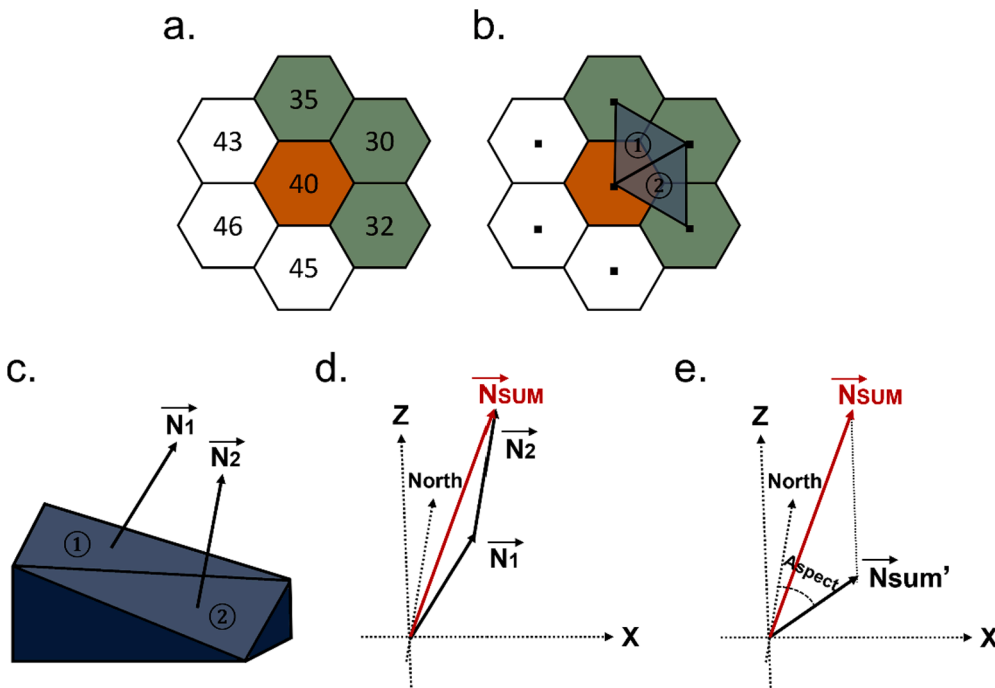


Fig. 6. Illustration of slope aspect calculation using the Multiple Downhill Neighbors method: a. elevations of the center cell and its first-ring neighbors where three downhill neighbors are in dark green, b. two triangular facets composed by three downhill neighbors, c. normal vectors  $\vec{N}_1$  and  $\vec{N}_2$  of two triangular facets, d.  $\vec{N}_{SUM}$  is the sum of normal vectors, which is the mean vector of two triangular facets, and e.  $\vec{N}_{SUM}'$  is the projection of the mean vector on the horizontal surface, and the aspect direction is the angle between  $\vec{N}_{SUM}'$  and true north. (For interpretation of the references to colour in this figure legend, the reader is referred to the web version of this article.)

where  $a, b, c, d, e, f,$  and  $g$  are the elevation values of a center cell and its neighbors, as shown in Fig. 5.

The BFP method fits a local plane surface accounting for each center cell plus its six neighboring cells by linear regression models, where the least-square method is used to minimize the sum of distances from the fitted plane to all input cell centroids (Travis, 1975; Fig. 5). The normal line of the fitted surface can be computed, and the slope gradient is then the angle between the normal line and the vertical axis, and the slope aspect is the compass direction of the projection of a reference vector, e. g., (0,0,1), onto the plane (Hodgson, 1998; Wright, 2017).

The MDN, FDA, and BFP methods allow returning arbitrary aspect angles ranging from 0 to 360°, whereas aspect angles computed by the MAG and MDG methods are bound to the six directions.

### 2.3.2. Curvature

Curvatures are essentially calculated as the second derivatives of the surface, which is a focal operation (Amatulli et al., 2020). In this research, we computed the curvature by projecting the rate of elevation changing rate along three native axes of hexagonal grids onto two orthogonal axes and combining two partial secondary derivatives as the final curvature value. The calculation follows the equations (Goldgof et al., 1989):

$$\text{curvature} = \frac{\sqrt{(dx^2)^2 + (dy^2)^2}}{\text{cell spacing}} \quad (10)$$

where  $dy^2$  and  $dx^2$  are the change of elevation differences along two orthogonal axes  $y$  and  $x$ , and are computed as.

$$dy^2 = di^2 + dj^2 \cdot \sin\frac{\pi}{6} - dk^2 \cdot \sin\frac{\pi}{6} \quad (11)$$

$$dx^2 = dj^2 \cdot \cos\frac{\pi}{6} + dk^2 \cdot \cos\frac{\pi}{6} \quad (12)$$

on even-resolution levels and.

$$dy^2 = di^2 \cdot \cos\frac{\pi}{6} + dj^2 \cdot \cos\frac{\pi}{6} \quad (13)$$

$$dx^2 = dk^2 + dj^2 \cdot \sin\frac{\pi}{6} - di^2 \cdot \sin\frac{\pi}{6} \quad (14)$$

on odd-resolution levels, where the change of elevation differences along three hexagonal axes  $i, k,$  and  $j$  are.

$$di^2 = 2 \times a - b - e \quad (15)$$

$$dk^2 = 2 \times a - c - f \quad (16)$$

$$dj^2 = 2 \times a - d - g \quad (17)$$

where  $a, b, c, d, e, f,$  and  $g$  are the elevation values of a center cell and its neighbors, as shown in Fig. 5.

### 2.3.3. Hill-shade

The inputs of the hill-shade function are local slope gradient and aspect, azimuth, and altitude. Therefore, producing hill-shade is a local operation and follows the computation methods used for traditional, rectangular terrain rasters. Hill-shade values of a cell can be calculated following the equation (Burrough and McDonell, 1998):

$$\text{Hillshade} = 255 \times \left( \cos\left(\frac{\pi}{2} - \text{altitude}\right) \times \cos(\text{gradient}) + \sin\left(\frac{\pi}{2} - \text{altitude}\right) \times \sin(\text{gradient}) \times \cos(\text{azimuth} - \text{aspect}) \right) \quad (18)$$

where altitude, azimuth, slope gradient, and slope aspect are in radians.

## 2.4. Topographic indices

Two topographic indices are produced: TRI and TPI. TRI presents the difference in elevation among the center cell's neighborhood, and TPI measures the difference between the center and the average of its neighboring cells (Guisan et al., 1999; Riley et al., 1999):

$$\text{TRI} = \sqrt{\sum (x_i - x_c)^2} \quad (19)$$

$$\text{TPI} = x_c - \frac{\sum x_i}{n} \quad (20)$$

where  $x_i$  is the elevation of each of the neighboring cells of the center cell  $x_c$ , and  $n$  is the number of neighboring cells. In this paper, computing topographic indices considered the first-ring-neighborhood for each center cell (Fig. 4), thus,  $n$  received a constant value of 6. Positive and negative TPI values represent the potential ridges and valleys in the terrain, respectively (Guisan et al., 1999). Because computing TRI and TPI requires neighboring cells to be involved, it is classified as a focal operation.

## 3. Experiment environment

The developed analytical functions in the ISEA3H DGGS were applied to three areas, each about 170 km<sup>2</sup>, with different levels of roughness in Alberta, around the regions of Buffalo Lake, the City of Calgary, and the Town of Canmore (Fig. 7). The Buffalo Lake area (112.85 to 113.00° W and 52.25 to 52.40° N) encompasses a watershed having the smoothest terrain surface where the elevation ranged from 799 to 850 m. The Canmore area (115.35 to 115.50° W and 51.15 to 51.30° N) is located in Alberta's Rocky Mountains and has the roughest terrain surface with 1360 to 2919 m elevations. The terrain in the Calgary region, an urban area (114.05 to 114.20° W and 51.05 to 51.20° N), is moderately rough compared to the other two areas, and the elevation ranges from 1043 to 1274 m.

The experiment was carried out on a machine with 8 cores, 12 GB memory, and 2x Intel(R) Xeon(R) CPU L5520 @ 2.27 GHz, by using Python 3.7.7 and R 3.6.2. All developed functionalities were tested on the ISEA3H DGGS from level 20 to 24 over three study areas. The experiment process ran in parallel using 8 cores, taking advantage of the discrete property of DGGS cells. The experiment scripts are available in the GitHub repository: <https://github.com/Erin-1919/Topographic-operations-DGGS>.

## 4. Experiment process and results

### 4.1. Data acquisition and quantization in DGGS

Canadian Digital Elevation Model (CDEM) data over three study areas were obtained at 0.75 arcsec resolution in the NAD83 CSRS reference system through the Geospatial Data Extraction portal in the GeoTIFF format (NRCan, 2017). Three study areas are in the same icosahedral face and are therefore in the same quad (i.e., the first quad; Fig. 2). In terms of the orientation relative to the Earth's surface, we set the longitude ( $\varphi$ ) of the pole, latitude ( $\lambda$ ) of the pole, and azimuth ( $\alpha$ ) as  $-51^\circ, 37^\circ,$  and  $0^\circ,$  respectively, so that grids over three study areas are oriented roughly toward true north. More discussion regarding the grid orientation is included in Section 5. Terrain data were modeled in the ISEA3H DGGS by resampling the original CDEM rasters over the cell centroid locations from level 20 to 24. Specifically, DGGS cell centroid locations were determined at each resolution, and a bilinear interpolation was used to estimate the elevation of the certain cell considering the nearest four central points of square-gridded rasters. Void values were assigned to the edge cells that did not have enough valid interpolation inputs. According to the previous quantitative evaluation, bilinear interpolation was recommended to quantize square-gridded remote-

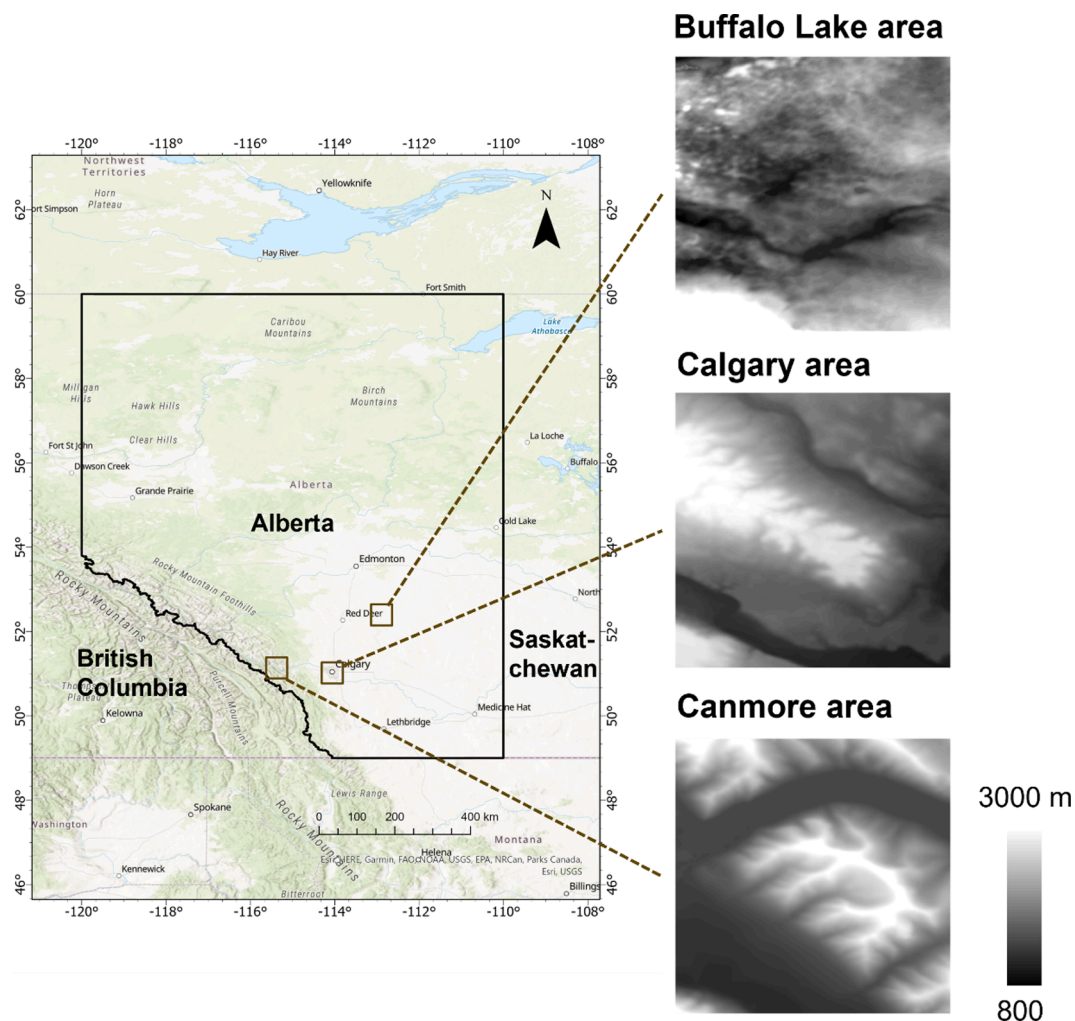


Fig. 7. The spatial locations and elevations of three study areas in Alberta, Canada in the World Geodetic System 1984 (WGS84) coordinate system (NRCan, 2015). (For interpretation of the references to colour in this figure legend, the reader is referred to the web version of this article.)

sensing imagery in hexagonal grids, which showed better information entropy, mutual information index, and deviation index, compared to other tested methods (Ma et al., 2021). The resolution level 24 with about 180.6 m<sup>2</sup> hexagonal cell area was the finest modeling level in this research, given that the CDEM data were achieved at 0.75 arcsec resolution which approximately equals 400 m<sup>2</sup> in cell area. A higher sample rate compared to the original sample rate of the CDEM helps to preserve the fidelity of the terrain signals (Li and Stefanakis, 2020; Shannon, 1949). Li et al. (2021) demonstrated that, following the Nyquist–Shannon sampling theorem, the difference between pre-DGGS and post-DGGS elevations of ground control points was minor at the finest resolution level by using such quantization method (Shannon, 1949). The precision, reflected by the decimal places of the modeled elevations, was gradually reduced at coarser DGGS resolution levels to maintain the rough ratio of the horizontal to vertical resolution, as suggested by Li et al. (2021). Parameters of the DGGS configuration used in the experiment are summarized in Table 1. The R library dgridR was used to locate the geographic locations of the cell centroids during the quantization process (Barnes and Sahr, 2017).

#### 4.2. Focal operations

##### 4.2.1. Focal statistics

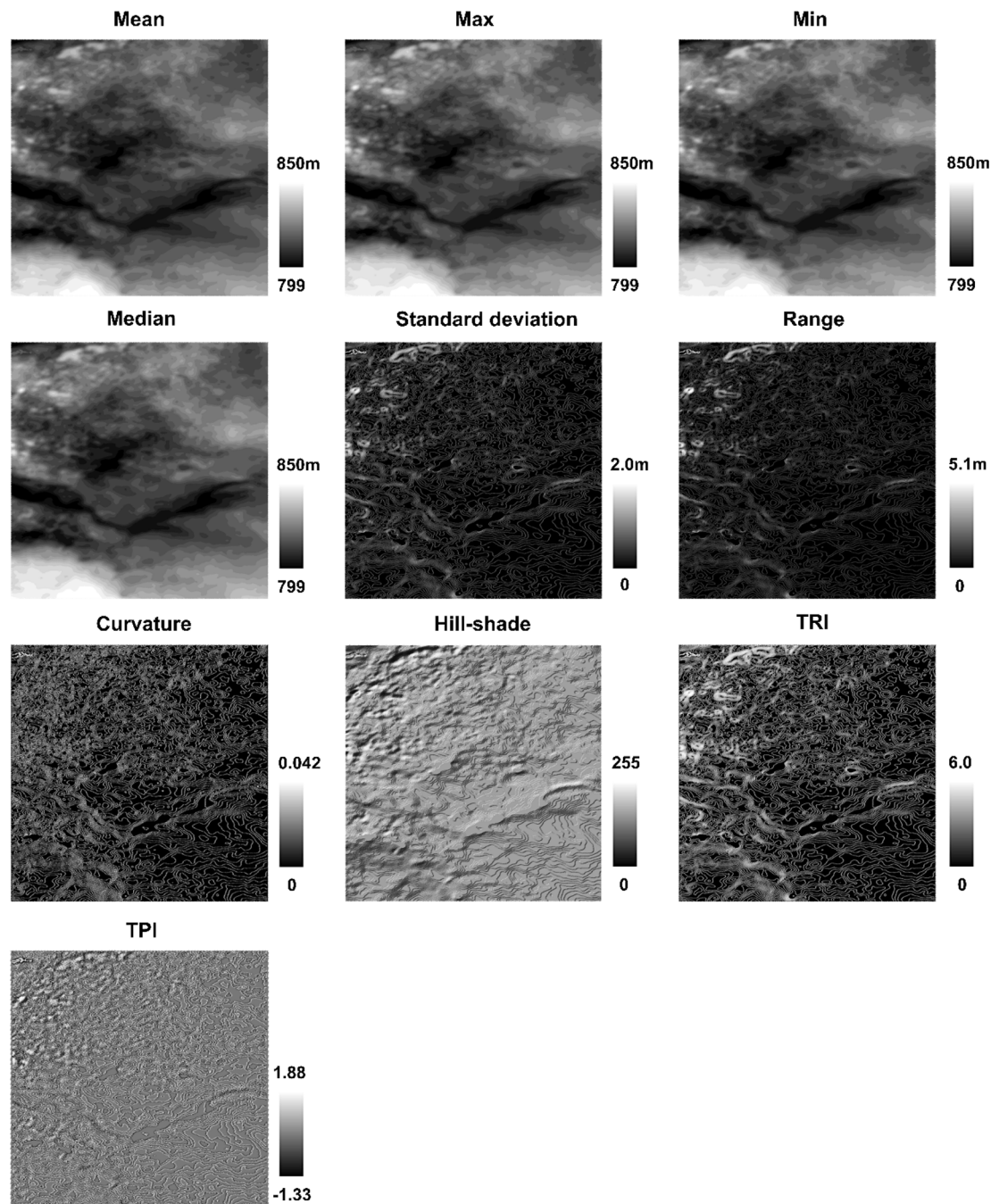
Focal statistics were tested by using 1–3 rings of hexagonal grids, namely the nearest 6, 12, and 18 hexagonal cells were used as the searching neighborhood, from level 20 to 24. Calculated statistics

Table 1

Parameters of DGGS configuration used in the experiment.

Parameter	Value
Tessellation	ISEA3H
Basic Platonic Solid	Icosahedron
Projection	Snyder equal area projection
Aperture	Three
Cell geometry	Hexagon
Orientation	Longitude of the pole ( $\varphi$ ) = $-51^\circ$ Latitude of the pole ( $\lambda$ ) = $37^\circ$ Azimuth ( $\alpha$ ) = $0^\circ$
Resolution levels and cell area	Cell area is about 14628.5 m <sup>2</sup> at level 20 Cell area is about 4876.2 m <sup>2</sup> at level 21 Cell area is about 1625.4 m <sup>2</sup> at level 22 Cell area is about 541.8 m <sup>2</sup> at level 23 Cell area is about 180.6 m <sup>2</sup> at level 24

included the mean, maximum, minimum, median, standard deviation, and range of the elevation values. Due to edge effects, where edge cells without a complete neighborhood were assigned null values for all statistics, the number of cells with valid statistical values was reduced with a larger searching neighborhood. Visualization of the focal statistics with the first-ring-neighborhood over three study areas at level 24 is available in Figs. 8–10. In this paper, computed results along with their hexagonal cell geometries were exported to Esri shapefile to be



**Fig. 8.** Visualization of focal statistics of elevations (mean, maximum, minimum, median, standard deviation, and range), curvature, hill-shade, Terrain Roughness Index (TRI), and Topographic Position Index (TPI) at level 24 in the Buffalo Lake area. Mean, maximum, minimum, and median elevations are visualized by hypsometric tinting whereas hill-shade is based on terrain shading.

visualized (ESRI, 1998).

#### 4.2.2. Slope gradient and aspect

Slope gradient was computed by five methods over three study areas. The BFP method cost the most computation time, followed by MDN, MAG and MDG, and FDA methods (Fig. 11). The maximum gradient was greater at finer resolutions in all areas no matter what method was used. This was the most apparent over the least rough area, Buffalo Lake, where the determined maximum slope gradient was 4.20 to 8.38° at level 20 and 8.72 to 17.33° at level 24 by different calculation methods (Table 2). The MDG, MDN, and FDA methods resulted in a greater mean slope gradient at finer levels in all areas (Table 2–4). The minimum gradient was 0 at all levels in three study areas.

To analyze to what extent the slope gradients calculated by different methods agreed with each other, we compared each of the methods pairwise by Pearson correlation coefficients ( $r$ ) across five resolution levels. In the Buffalo Lake area, high correlation coefficients ( $r > 0.9$ ) were observed between five methods. In the Calgary and Canmore areas, the calculated Pearson correlation coefficients of slope gradient were all higher than 0.8. In other words, the slope gradient calculated by different methods had stronger, positive relationships among all resolutions. The visualized slope gradient by five methods in three study areas at level 24 is shown in Fig. 12.

The slope aspect was computed along with the gradient by five methods. Because the aspect was not a linear measurement, the direct quantitative analysis of aspect degree was not included in this paper.

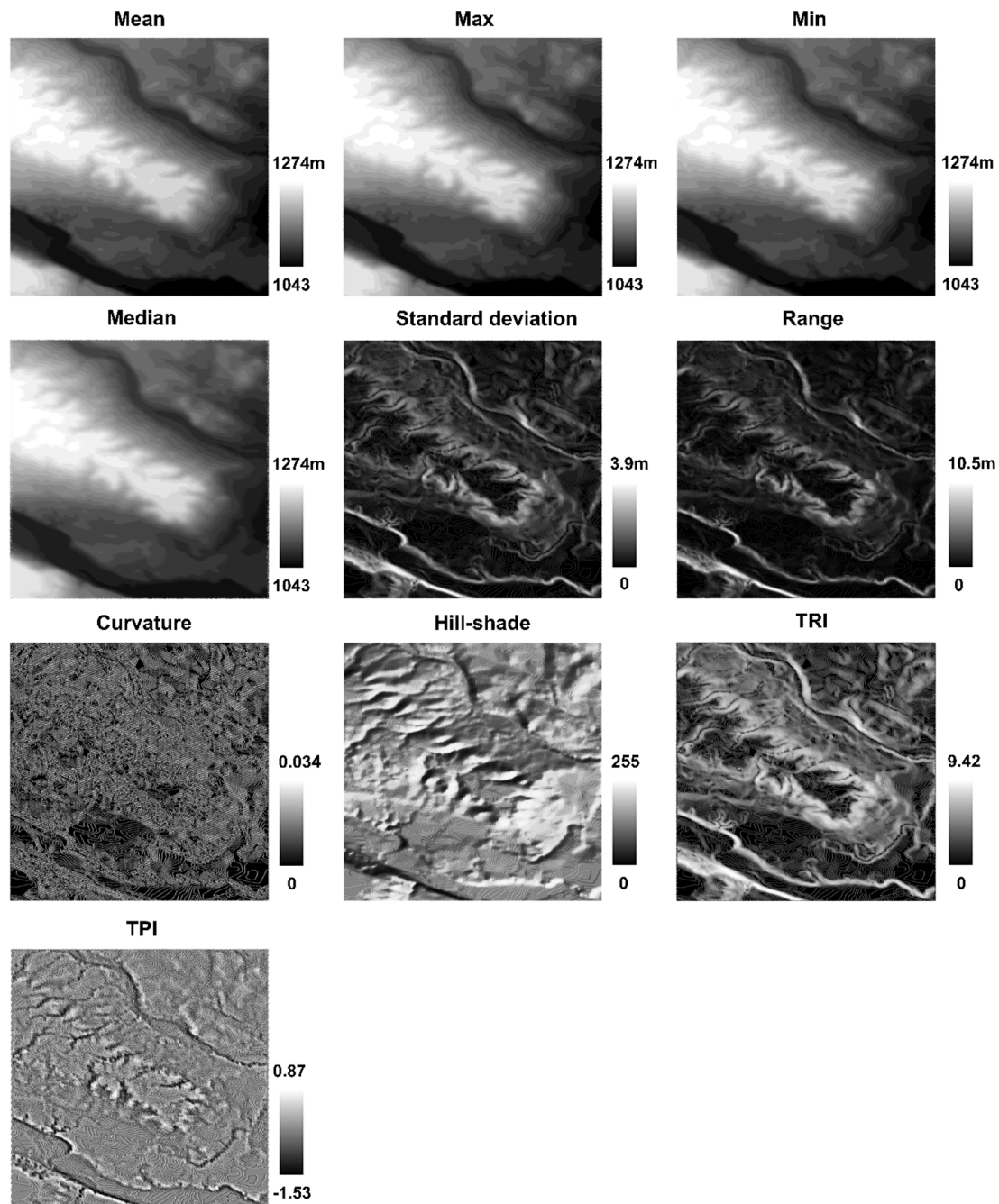


**Fig. 9.** Visualization of focal statistics of elevations (mean, maximum, minimum, median, standard deviation, and range), curvature, hill-shade, Terrain Roughness Index (TRI), and Topographic Position Index (TPI) at level 24 in the Calgary area. Mean, maximum, minimum, and median elevations are visualized by hypsometric tinting whereas hill-shade is based on terrain shading.

Nonetheless, Li et al. (2022) generated flow routing grids based on these five algorithms in the ISEA3H DGGS and found that the flow directions, essentially aspect directions, can vary among different methods. Such variation can propagate to the flow-up hydrological parameter production such as flow accumulation, upslope contributing area, and hydrological indices, reflected by both the cell-wise comparison and visualization (Li et al., 2022).

#### 4.2.3. Curvature

Curvature was calculated based on the first-ring neighborhood. Generally, a greater changing rate of the slope was identified at finer resolution levels in rougher areas. The highest mean curvature was observed at level 24, which were 0.002, 0.003, and 0.004 in the Buffalo

Lake, Calgary, and Canmore areas, respectively, with all achieving calculated standard errors of mean less than 0.0005 (Table 5). Across levels 20 to 24, the maximum curvature ranged from 0.002 to 0.042 in the Buffalo Lake area, 0.003 to 0.034 in the Calgary area, and 0.019 to 0.460 in the Canmore area, with finer resolutions corresponding to higher curvature (Table 5). The minimum curvature was 0 over the levels, meaning no change in the slope. Calculated curvature at level 24 in three study areas is visualized in Figs. 8–10.

#### 4.2.4. TRI

TRI was computed following Eq. (19) within the first-ring-neighborhood. Higher values were observed at coarser resolution levels in rougher areas. Mean TRI values were 2.89, 10.10, and 86.96 at

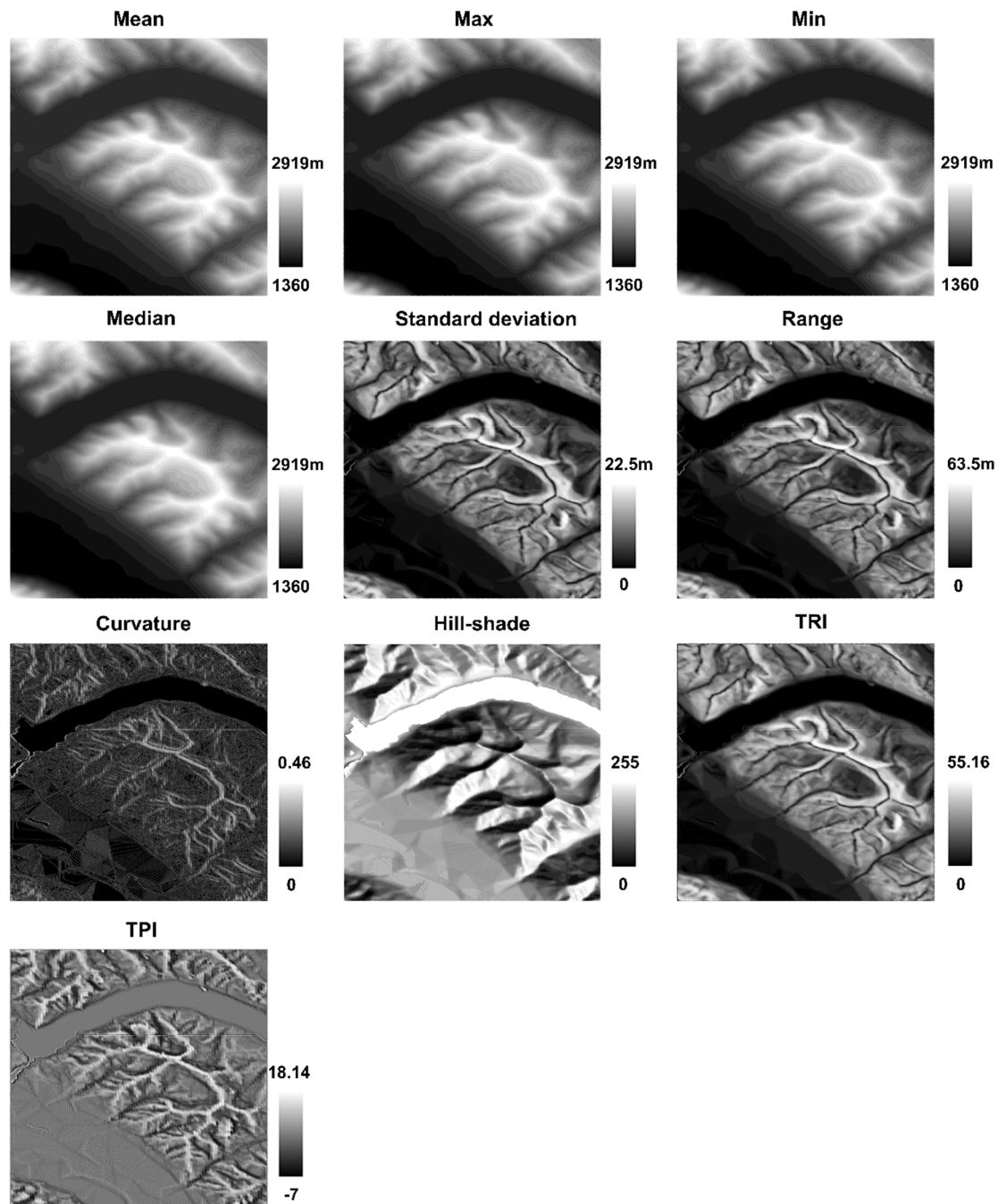


**Fig. 10.** Visualization of focal statistics of elevations (mean, maximum, minimum, median, standard deviation, and range), curvature, hill-shade, Terrain Roughness Index (TRI), and Topographic Position Index (TPI) at level 24 in the Canmore area. Mean, maximum, minimum, and median elevations are visualized by hypsometric tinting whereas hill-shade is based on terrain shading.

level 20, and 0.40, 1.19, and 9.63 at level 24 in the Buffalo Lake, Calgary, and Canmore areas, respectively, with higher standard error of mean in coarser levels (Table 5). The minimum TRI value was 0 at all levels, representing flat areas. TRI in three study areas at level 24 is visualized in Figs. 8–10.

#### 4.2.5. TPI

Based on Eq. (20), TPI was calculated to measure the difference between the center cell and the average of its six neighbors. TPI can be positive or negative, and 0 represents flat areas. Higher absolute values were generally found at coarser levels in rougher areas. The values ranged from  $-4.30$  to  $7.77$  at level 20 and  $-1.33$  to  $1.88$  at level 24 in the Buffalo Lake area, ranged from  $-9.57$  to  $9.47$  at level 20 and  $-1.53$

to  $0.87$  at level 24 in the Calgary area, and ranged from  $-43.95$  to  $64.87$  at level 20 and  $-7.00$  to  $18.14$  at level 24 in the Canmore area (Table 5). Visualization of TPI over three tested areas at level 24 is available in Figs. 8–10.

#### 4.3. Local operations

In our implementation, the hill-shade parameters azimuth and altitude in Eq. (18) were set with default values of  $315^\circ$  and  $45^\circ$ , respectively. The slope gradient and slope aspect used to generate hill-shade were based on the FDA method because it cost the shortest computation time in our experiment (Fig. 11). Visualization of the hill-shade over three study areas at level 24 is shown in Figs. 8–10.

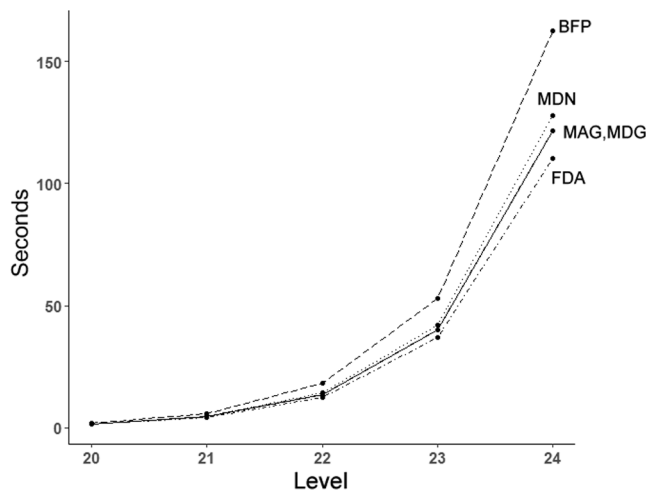


Fig. 11. The average time consumed in calculating slope gradient and aspect by the Maximum Adjacent Gradient (MAG), Maximum Downward Gradient (MDG), Multiple Downhill Neighbors (MDN), Finite-Difference Algorithm (FDA), and Best-Fit Plane (BFP) methods over three study areas from level 20 to 24.

Table 2 Slope gradient calculated by five algorithms in the Buffalo Lake area (unit: °).

		Level 20	Level 21	Level 22	Level 23	Level 24
Maximum Adjacent Gradient	Max	8.38	9.06	10.18	10.99	16.51
	Mean	0.92	0.99	1.11	1.22	1.25
	Standard error of mean	0.01	0.00	0.00	0.00	0.00
Maximum Downward Gradient	Max	8.38	9.06	10.18	10.99	16.51
	Mean	0.65	0.71	0.75	0.77	0.81
	Standard error of mean	0.01	0.00	0.00	0.00	0.00
Multiple Downhill Neighbors	Max	4.59	6.85	7.06	8.15	12.01
	Mean	0.49	0.55	0.58	0.57	0.57
	Standard error of mean	0.00	0.00	0.00	0.00	0.00
Finite-Difference Algorithm	Max	7.34	12.12	14.38	15.61	17.33
	Mean	0.94	1.08	1.15	1.18	1.22
	Standard error of mean	0.01	0.00	0.00	0.00	0.00
Best-Fit Plane	Max	4.20	6.97	8.18	8.55	8.72
	Mean	0.34	0.31	0.23	0.16	0.11
	Standard error of mean	0.00	0.00	0.00	0.00	0.00

4.4. Zonal operations

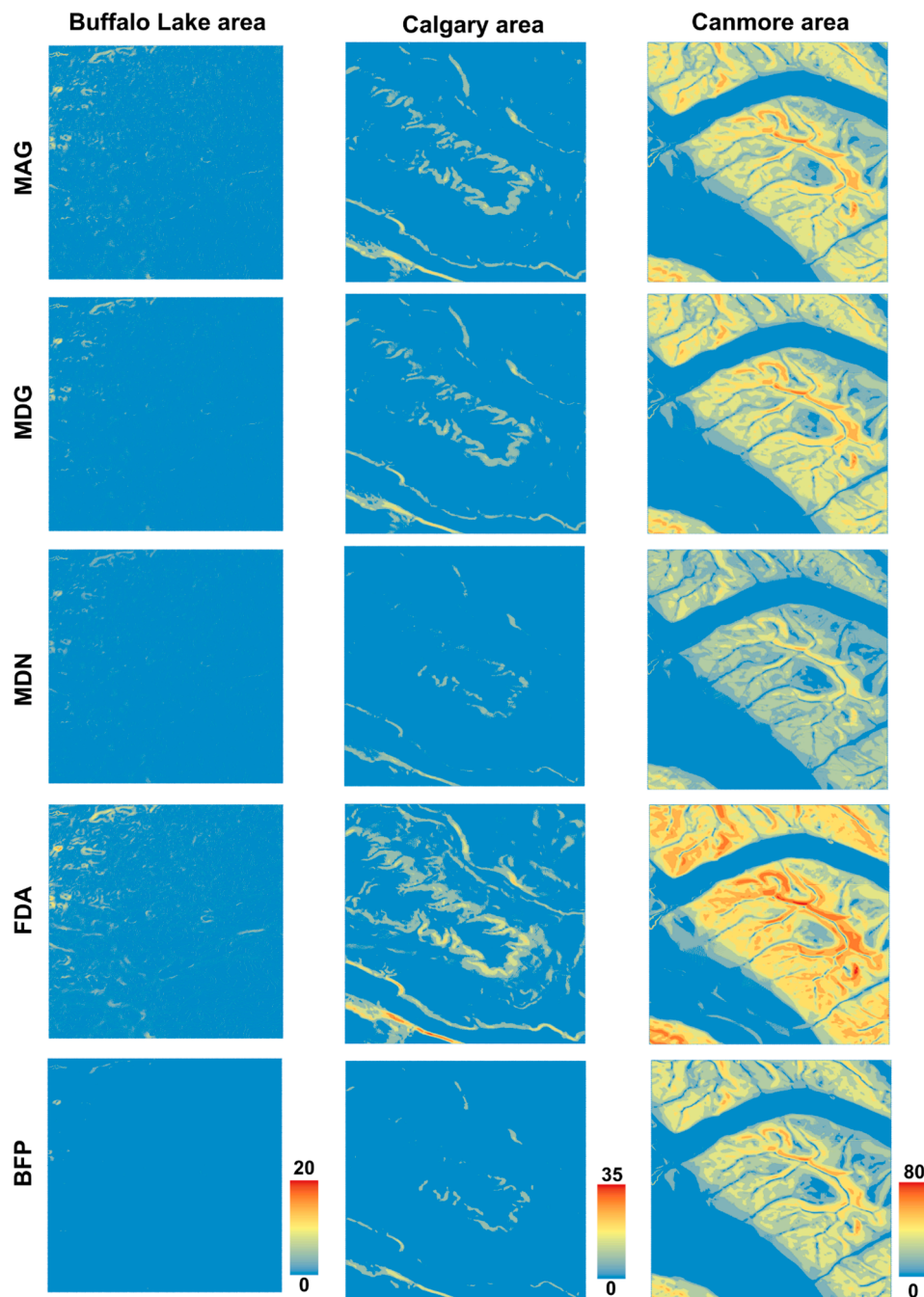
We used the classification raster of the 2020 Annual Crop Inventory produced by the Agriculture and Agri-Food Canada as an example to partition the zones (AAFC, 2020). The map was created by decision trees based on multiple satellite image series and showed the spatial distribution of crop and vegetation types in Canada with integer codes representing classifications. The classification raster was quantized in the ISEA3H DGGS over three study areas from level 20 to 24 by nearest

Table 3 Slope gradient calculated by five algorithms in the Calgary area (unit: °).

		Level 20	Level 21	Level 22	Level 23	Level 24
Maximum Adjacent Gradient	Max	18.51	21.26	20.79	22.08	21.89
	Mean	3.11	3.03	2.99	3.11	3.24
	Standard error of mean	0.02	0.01	0.01	0.00	0.00
Maximum Downward Gradient	Max	18.51	21.26	20.79	22.08	21.89
	Mean	2.52	2.58	2.59	2.63	2.69
	Standard error of mean	0.02	0.01	0.01	0.00	0.00
Multiple Downhill Neighbors	Max	13.20	14.63	15.41	15.43	17.67
	Mean	1.71	1.76	1.79	1.80	1.82
	Standard error of mean	0.01	0.01	0.00	0.00	0.00
Finite-Difference Algorithm	Max	26.32	28.46	30.33	31.36	31.56
	Mean	3.81	3.96	4.03	4.06	4.11
	Standard error of mean	0.03	0.02	0.01	0.01	0.00
Best-Fit Plane	Max	15.93	17.34	18.57	19.11	18.74
	Mean	2.08	2.02	1.80	1.44	1.01
	Standard error of mean	0.02	0.01	0.01	0.00	0.00

Table 4 Slope gradient calculated by five algorithms in the Canmore area (unit: °).

		Level 20	Level 21	Level 22	Level 23	Level 24
Maximum Adjacent Gradient	Max	65.16	65.02	67.24	65.52	67.39
	Mean	22.34	21.60	21.11	20.76	20.66
	Standard error of mean	0.15	0.08	0.05	0.03	0.02
Maximum Downward Gradient	Max	65.16	65.02	67.24	65.52	67.39
	Mean	19.35	19.72	19.92	19.97	20.06
	Standard error of mean	0.14	0.08	0.05	0.03	0.02
Multiple Downhill Neighbors	Max	55.50	60.41	57.88	61.76	58.31
	Mean	13.44	13.71	13.85	13.85	13.90
	Standard error of mean	0.10	0.06	0.03	0.02	0.01
Finite-Difference Algorithm	Max	70.85	72.99	74.08	74.42	74.47
	Mean	27.17	27.66	27.84	27.92	27.95
	Standard error of mean	0.18	0.10	0.06	0.03	0.02
Best-Fit Plane	Max	58.98	62.08	63.70	64.21	64.27
	Mean	17.84	18.22	18.30	18.15	17.75
	Standard error of mean	0.12	0.07	0.04	0.03	0.01



**Fig. 12.** Visualization of the slope gradient calculated by the Maximum Adjacent Gradient (MAG), Maximum Downward Gradient (MDG), Multiple Downhill Neighbors (MDN), Finite-Difference Algorithm (FDA), and Best-Fit Plane (BFP) methods at level 24 in three study areas. (For interpretation of the references to colour in this figure legend, the reader is referred to the web version of this article.)

neighbor resampling. The mean, maximum, minimum, median, standard deviation, and range of the elevation values were calculated among classification zones over three study areas. The statistics results among zones of shrubland, wetland, grassland, coniferous forest, broadleaf forest, and mixed-wood forest at level 24 are summarized in Table 6.

## 5. Discussion

### 5.1. Aspect directions in DGGS

Due to the nature of the ISEA3H tessellation, a relative  $30^\circ$  rotation of the hexagonal grids exists between each successive level (Sahr, 2008). Therefore, the direction bins of the anisotropic slope aspect were

different at odd-resolution and even-resolution levels. The unrestricted slope aspect calculated using the MDN, FDA, and BFP methods was less affected by grid axes' shifts. In terms of hexagonal grids with other aperture, a relative  $19.1^\circ$  rotation of the axes exists in an aperture 7 hexagonal grid between successive resolutions, while an aperture 4 hexagonal grid is free of axes rotation among resolution levels (Sahr, 2019).

In addition, the definition of the aspect directions in this paper can be different than the true understanding of the terrain aspect which is defined as the compass direction relative to true north (Skidmore, 1989). Instead, we used the direction to which grids within a certain area of interest are orientated as the referenced north. As Florinsky (1998) suggested, local attributes such as slope gradient and aspect are

**Table 5**  
Curvature, Terrain Roughness Index (TRI), and Topographic Position Index (TPI) in three study areas from level 20 to 24.

		Curvature			TRI			TPI	
		Max	Mean	SEM <sup>1</sup>	Max	Mean	SEM	Max	Min
Buffalo Lake area	20	0.002	0.000	0.000	25.10	2.89	0.02	7.77	-4.30
	21	0.004	0.000	0.000	17.27	1.82	0.01	4.84	-2.94
	22	0.008	0.001	0.000	11.83	1.14	0.00	3.13	-2.59
	23	0.016	0.001	0.000	7.42	0.69	0.00	2.20	-1.78
	24	0.042	0.002	0.000	6.00	0.40	0.00	1.88	-1.33
Calgary area	20	0.003	0.000	0.000	68.35	10.10	0.07	9.47	-9.57
	21	0.004	0.000	0.000	43.26	5.84	0.03	4.26	-4.45
	22	0.006	0.001	0.000	26.92	3.40	0.01	1.91	-2.19
	23	0.014	0.001	0.000	16.20	2.01	0.00	1.04	-1.74
	24	0.034	0.003	0.000	9.42	1.19	0.00	0.87	-1.53
Canmore area	20	0.019	0.002	0.000	401.74	86.96	0.63	64.87	-43.95
	21	0.024	0.002	0.000	260.82	50.18	0.21	29.32	-20.20
	22	0.059	0.003	0.000	161.18	28.91	0.07	22.11	-12.63
	23	0.127	0.003	0.000	95.23	16.68	0.02	17.91	-6.63
	24	0.460	0.004	0.000	55.16	9.63	0.01	18.14	-7.00

<sup>1</sup> SEM stands for standard error of mean.

**Table 6**  
Zonal statistics of the elevation values among crop and vegetation classification zones in three study areas at level 24.

		Mean	Maximum	Minimum	Median	Standard deviation	Range
Buffalo Lake area	Shrubland	814.3	844.0	799.0	813.9	6.4	45.0
	Wetland	813.3	849.6	799.0	812.1	7.0	50.6
	Grassland	814.1	849.1	799.0	813.0	6.9	50.1
	Coniferous	814.1	848.0	799.0	813.3	7.3	49.0
	Broadleaf	815.1	850.0	799.0	815.0	6.6	51.0
	Mixed-wood	814.3	835.0	802.0	814.0	5.8	33.0
Calgary area	Shrubland	1144.9	1264.8	1046.0	1128.5	55.7	218.8
	Wetland	1144.7	1268.0	1044.0	1121.0	55.6	224.0
	Grassland	1167.0	1268.0	1049.4	1171.9	50.7	218.6
	Coniferous	1141.5	1273.0	1044.0	1124.5	57.6	229.0
	Broadleaf	1156.7	1268.5	1045.0	1161.1	55.2	223.5
	Mixed-wood	1148.4	1251.4	1045.0	1154.0	57.0	206.4
Canmore area	Shrubland	1793.6	2369.2	1360.0	1765.4	279.1	1009.2
	Wetland	1644.5	2494.5	1360.0	1529.9	283.2	1134.5
	Grassland	1963.6	2505.8	1364.6	1961.9	295.2	1141.2
	Coniferous	1672.8	2712.0	1381.3	1606.9	242.1	1330.7
	Broadleaf	1655.8	2479.8	1360.0	1520.0	299.6	1119.8
	Mixed-wood	1832.7	2669.5	1360.0	1826.4	294.1	1309.5

mathematical variables rather than real-world values. When the orientation of the DGGS relative to the Earth’s surface is configured so that the grids within the study area are orientated to an unneglectable angle to the true north, then a constant angle needs to be added to the calculated aspect direction, if a true aspect value is desired. Moreover, the area of interest can be so large that the cell orientation within the area of interest cannot be ignored. This situation was not explored here and is left for future study.

5.2. Comparison between slope calculation methods

Among the five methods to calculate the slope gradient and aspect, the MAG and MDG algorithms produced restricted, discrete aspect directions while the MDN, FDA, and BFP algorithms contributed to unrestricted, continuous aspect values. The FDA is computationally the most efficient algorithm, while the BFP turns out to be the most computationally expensive algorithm. In addition, when calculating the slope using the MDG or MDN algorithms, it is possible that the center cell does not have any neighbors with lower elevations, a situation that we treated by increasing the cell elevation to that of its lowest neighbors

and by assigning the slope gradient value 0. However, the other three methods (i.e., MAG, FDA, and BFP) were less sensitive to such scenarios when computing the slope gradient and aspect and they can all be applied to a surface with small depressions. Nonetheless, a smoothing filter before calculating slope gradient or aspect was recommended to eliminate small depressions and peaks no matter what algorithm is applied (Srinivasan and Engel, 1991). This can be done by focal statistics developed in this research, namely, producing the mean value in the neighborhood for each center cell.

Previous studies evaluated slope calculation methods by comparing results to known ground values or assuming that one method of determining slope gradient and aspect produced true values (Hodgson, 1998; Skidmore, 1989). Guth (1995) noticed that different algorithms can vary the average slope by as much as 25%. In this study, various methods were compared using Pearson correlation coefficients calculated in terms of slope gradient, and the values were highly and positively related among five methods across multiple resolutions. Nonetheless, the slope aspect angles were not compared directly in this study, and the potential differences can propagate these uncertainties to the computation of, for example, flow directions and flow accumulation (Li et al.,

2022).

### 5.3. Influences of DGGs resolutions

Slope gradient and curvature are the first and second derivatives of a surface, where the discrete differences are normalized by the cell size. Overall, both the computed slope gradient and curvature were found to increase at finer modeling levels in this study. The observations were mainly due to the smoothing of the modeled terrain at coarser resolutions (Vázquez and Feyen, 2007). This was partially in line with the previous research on traditional DEM which found that the slope gradient decreased as DEM cells aggregated to coarser resolutions, although there was not a clear tendency of curvature with regard to resolutions (Wu et al., 2008). Nonetheless, the produced TRI and TPI which measured the difference between the center cell and its neighborhood without normalization tended to be higher at coarser modeling levels, in terms of their absolute values. We also noticed that the smooth area had more sensitivity to modeling resolutions regarding the slope gradient, which suggested that an appropriate modeling resolution depends on the terrain surface complexity. For example, a fine resolution can benefit modeling a mountainous area while it is not necessarily required for a flat landscape (Hengl and Evans, 2009; Shannon, 1949; Wu et al., 2008).

### 5.4. Study impact

This work reviewed a few topographic analysis algorithms on rectangular grids and explored their application using a hexagonal DGGs. The concepts of the developed algorithms can be used in other DGGs where the cell geometry is a hexagon, for instance, hierarchical grids with four or seven as the refinement ratio among levels, as long as an indexing system is available to support the neighbor navigation. In addition, we reviewed five methods to calculate slope gradient and aspect in the ISEA3H DGGs, and pair-wisely compared them over multiple granularities and areas. Analysis of other hexagonal tessellations with an aperture of four or seven should reveal a more apparent impact from resolution levels because of their more rapid change of cell size across levels. This research also helped to bridge the gap between the existing DGGs implementations and the DGGs-driven decision-making in the future. For example, topographic parameters and topographic indices are commonly used as influencing factors in ecological modeling, environmental mapping, and disaster prediction (Esfandiari et al., 2020; Zhao et al., 2019). The proposed methods for producing these parameters or indices, together with the data integration ability, will contribute to effective cell-based predictive modeling in a pure DGGs environment.

## 6. Conclusions

This study developed analytical operations for modeled terrain data in a pure ISEA3H DGGs environment and discussed them by three categories, namely focal, local, and zonal operations. The developed functions included focal statistics, zonal statistics, topographic parameters such as slope gradient and aspect, curvature, hill-shade, and two topographic indices. Five methods to generate slope gradient and aspect on a hexagonal grid were reviewed and demonstrated in a hexagonal grid, and the experiments were carried out over three areas with different roughness across five resolution levels. Results showed that the FDA method produced continuous aspect direction values, was free from pre-smoothing operations, and cost the least computation time. Although the averaged slope gradient values did not highly agree among the five methods, the cell-based, pair-wise comparison of the slope gradient showed strong positive relationships between each two of the methods. We also noticed that higher slope gradient and curvature values while lower TRI and TPI values were determined at finer resolutions. A fine resolution level was not always recommended, especially

over a flat terrain surface. This research demonstrated the multi-resolution terrain analysis in a hexagonal DGGs and is useful for further application of DGGs to support decision-making in the real world.

### CRedit authorship contribution statement

**Mingke Li:** Conceptualization, Methodology, Software, Formal analysis, Investigation, Writing – original draft, Visualization. **Heather McGrath:** Conceptualization, Methodology, Investigation, Resources, Writing – review & editing, Supervision. **Emmanuel Stefanakis:** Conceptualization, Methodology, Investigation, Resources, Writing – review & editing, Supervision.

### Declaration of Competing Interest

The authors declare that they have no known competing financial interests or personal relationships that could have appeared to influence the work reported in this paper.

### Acknowledgements

We acknowledge the funding from the Canadian Natural Sciences and Engineering Research Council (NSERC) Discovery Grant program (Grant Number: RGPIN/03977-2019) and the De l'observation de la terre aux services d'information décisionnelle (CREATE DOTS) program.

### References

- AAFC, 2020. Annual Crop Inventory, <https://open.canada.ca/data/en/dataset/ba2645d5-4458-414d-b196-6303ac06c1c9> (accessed 10 October 2021).
- Alderson, T., Purs, M., Du, X., Mahdavi-Amiri, A., Samavati, F., 2020. Digital earth platforms, in: Guo, H., Goodchild, M., Annoni, A. (Eds.), *Manual of digital earth*. Springer, Singapore, pp. 25–54.
- Amatulli, G., McInerney, D., Sethi, T., Strobl, P., Domisch, S., 2020. Geomorpho90m, empirical evaluation and accuracy assessment of global high-resolution geomorphometric layers. *Sci Data* 7, 162. <https://doi.org/10.1038/s41597-020-0479-6>.
- Barnes, R., Sahr, K., 2017. dggridR: Discrete Global Grids for R. R package version 2.0.4, <https://github.com/r-barnes/dggridR> (accessed 5 March 2020).
- Bernardin, T., Cowgill, E., Kreylos, O., Bowles, C., Gold, P., Hamann, B., Kellogg, L., 2011. Crusta: a new virtual globe for real-time visualization of sub-meter digital topography at planetary scales. *Comput. Geosci.* 37 (1), 75–85. <https://doi.org/10.1016/j.cageo.2010.02.006>.
- Burrough, P.A., McDonnell, R.A., 1998. *Principles of Geographical Information Systems*. Oxford University Press, New York, NY, USA.
- Dunn, M., Hickey, R., 1998. The effect of slope algorithms on slope estimates within a GIS. *Cartography* 27 (1), 9–15. <https://doi.org/10.1080/00690805.1998.9714086>.
- Dutton, G., 1984. Part 4: mathematical, algorithmic and data structure issues: geodesic modelling of planetary relief. *Cartographica* 21 (2-3), 188–207. <https://doi.org/10.3138/R613-191U-7255-082N>.
- Dutton, G., 1999. *A hierarchical coordinate system for geoprocessing and cartography: working through the scales*. Springer-Verlag, Berlin, Germany.
- Esfandiari, M., Jabari, S., McGrath, H., Coleman, D., 2020. Flood mapping using random forest and identifying the essential conditioning factors: a case study in Fredericton, New Brunswick, Canada. *ISPRS Ann. Photogramm. Remote Sens. Spat. Inf. Sci.* V-3-2020, 609–615. [10.5194/isprs-annals-V-3-2020-609-2020](https://doi.org/10.5194/isprs-annals-V-3-2020-609-2020).
- ESRI, 1998. ESRI shapefile technical description, <http://www.esri.com/library/whitepapers/pdfs/shapefile.pdf>.
- Florinsky, I.V., 1998. Accuracy of local topographic variables derived from digital elevation models. *Int. J. Geogr. Inf. Sci.* 12 (1), 47–62. <https://doi.org/10.1080/136588198242003>.
- Foster, I., Kesselman, C., Tuecke, S., 2001. The anatomy of the grid: enabling scalable virtual organizations. *Int. J. High Perform. Comput. Appl.* 15 (3), 200–222. <https://doi.org/10.1177/109434200101500302>.
- Goldgof, D.B., Huang, T.S., Lee, H., 1989. A curvature-based approach to terrain recognition. *IEEE Trans. Pattern Anal. Mach. Intell.* 11, 1213–1217. <https://doi.org/10.1109/34.42859>.
- Guisan, A., Weiss, S.B., Weiss, A.D., 1999. GLM versus CCA spatial modeling of plant species distribution. *Plant Ecol.* 143, 107–122. <https://doi.org/10.1023/A:1009841519580>.
- Guth, P.L., 1995. *Slope and aspect calculations on gridded digital elevation models: examples from a geomorphometric toolbox for personal computers*. *Zeitschrift für Geomorphol.* 101, 31–52.
- Hengl, T., Evans, I.S., 2009. Mathematical and digital models of the land surface, in: Reuter, H.I., Hengl, T. (Eds.), *Geomorphometry-concepts, software, applications*.

- Elsevier Science, Institute for Environment and Sustainability (European Commission. Joint Research Centre), Hungary, pp. 31–63.
- Hodgson, M.E., 1998. Comparison of angles from surface slope/aspect algorithms. *CaGIS* 25 (3), 173–185. <https://doi.org/10.1559/152304098782383106>.
- Hodgson, M.E., Gaile, G., 1996. Characteristic mean and dispersion in surface orientations for a zone. *Int. J. Geogr. Inf. Syst.* 10, 817–830. <https://doi.org/10.1080/02693799608902111>.
- ISO, 2021. ISO 19170-1:2021 Geographic information — Discrete Global Grid Systems Specifications — Part 1: Core Reference System and Operations, and Equal Area Earth Reference System, <https://www.iso.org/standard/32588.html> (accessed 10 December 2021).
- Li, M., McGrath, H., Stefanakis, E., 2021. Integration of heterogeneous terrain data into Discrete Global Grid Systems. *CaGIS* 48 (6), 546–564. <https://doi.org/10.1080/15230406.2021.1966648>.
- Li, M., McGrath, H., Stefanakis, E., 2022. Geovisualization of hydrological flow in hexagonal grid systems. *Geographies* 2, 227–244. <https://doi.org/10.3390/geographies2020016>.
- Li, M., Stefanakis, E., 2020. Geospatial operations of discrete global grid systems—a comparison with traditional GIS. *J. Geovis. Spat. Anal.* 4, 26. <https://doi.org/10.1007/s41651-020-00066-3>.
- Ma, Y., Li, G., Yao, X., Cao, Q., Zhao, L., Wang, S., Zhang, L., 2021. A precision evaluation index system for remote sensing data sampling based on hexagonal discrete grids. *ISPRS Int. J. Geo-Inf.* 10, 3. <https://doi.org/10.3390/ijgi10030194>.
- Mahdavi-Amiri, A., Alderson, T., Samavati, F., 2015. A survey of digital earth. *Comput. Graph.* 53, 95–117. <https://doi.org/10.1016/j.cag.2015.08.005>.
- NRCan, 2015. Canadian Digital Elevation Model, 1945–2011. In: Canada Centre for Mapping and Earth Observation, S.P.A.R.S., Natural Resources Canada, Government of Canada (Ed.). Canada Centre for Mapping and Earth Observation, Strategic Policy and Results Sector, Natural Resources Canada, Government of Canada.
- NRCan, 2017. Geospatial data extraction, <https://maps.canada.ca/czs/index-en.html> (accessed 15 October 2020).
- OGC, 2017. Topic 21: discrete global grid system abstract specification, <http://www.opengis.net/doc/AS/dggs/1.0> (accessed 15 November 2019).
- OpenEAGGR, 2017. Open Equal Area Global GRid, <https://github.com/riskaware-ltd/op-en-eaggr> (accessed 26 November 2019).
- Raposo, P., C. Robinson, A., Brown, R., 2019. A virtual globe using a Discrete Global Grid System to illustrate the modifiable areal unit problem. *Cartographica* 54, 51–62. <https://doi.org/10.3138/cart.54.1.2018-0015>.
- Raposo, P., 2019. Geovisualization of complex origin-destination flow maps using Discrete Global Grid Systems. In: 29th International Cartographic Conference (ICC 2019). International Cartographic Association, Tokyo, Japan.
- Rawson, A., Sabeur, Z., Brito, M., 2021. Intelligent geospatial maritime risk analytics using the Discrete Global Grid System. *Big Earth Data* 1–29. <https://doi.org/10.1080/20964471.2021.1965370>.
- Riley, S.J., DeGloria, S.D., Elliot, R., 1999. Index that quantifies topographic heterogeneity intermountain. *J. Sci.* 5, 23–27.
- Robertson, C., Chaudhuri, C., Hojati, M., Roberts, S.A., 2020. An integrated environmental analytics system (IDEAS) based on a DGGs. *ISPRS J. Photogramm. Remote Sens.* 162, 214–228. <https://doi.org/10.1016/j.isprsjprs.2020.02.009>.
- Sahr, K., 2008. Location coding on icosahedral aperture 3 hexagon discrete global grids. *Comput. Environ. Urban Syst.* 32 (3), 174–187. <https://doi.org/10.1016/j.compenvurbysys.2007.11.005>.
- Sahr, K., 2019. Central place indexing: hierarchical linear indexing systems for mixed-aperture hexagonal discrete global grid systems. *Cartographica* 54 (1), 16–29. <https://doi.org/10.3138/cart.54.1.2018-0022>.
- Sahr, K., White, D., Kimerling, A.J., 2003. Geodesic Discrete Global Grid Systems. *CaGIS* 30 (2), 121–134. <https://doi.org/10.1559/152304003100011090>.
- Shanholtz, V.O., Desai, C.J., Zhang, N., Kleene, J.W., Metz, C.D., Flagg, J.M., 1990. Hydrologic/water quality modeling in a GIS environment. *ASAE* 90, 3033.
- Shannon, C.E., 1949. Communication in the presence of noise. *Proc. IRE Proc. IRE* 37 (1), 10–21.
- Shorridge, A.M., 2004. Geometric variability of raster cell class assignment. *Int. J. Geogr. Inf. Sci.* 18 (6), 539–558.
- Skidmore, A.K., 1989. A comparison of techniques for calculating gradient and aspect from a gridded digital elevation model. *Int. J. Geogr. Inf. Syst.* 3 (4), 323–334. <https://doi.org/10.1080/02693798908941519>.
- Srinivasan, R., Engel, B.A., 1991. Effect of slope prediction methods on slope and erosion estimates. *Appl. Eng.* 7, 779–783. <https://doi.org/10.13031/2013.26302>.
- Tomlin, C.D., 1990. *Geographic Information Systems and cartographic modeling*. Prentice Hall College Div, California, USA.
- Travis, M.R., 1975. VIEWIT: computation of seen areas, slope, and aspect for land-use planning. Department of Agriculture, Forest Service, Pacific Southwest Forest and Range Experiment Station, Rep. PSW 11/1975.
- Uber, 2017. H3: a hexagonal hierarchical geospatial indexing system, <https://github.com/uber/h3> (accessed 25 November 2019).
- Vázquez, R.F., Feyen, J., 2007. Assessment of the effects of DEM gridding on the predictions of basin runoff using MIKE SHE and a modelling resolution of 600 m. *J. Hydrol.* 334 (1–2), 73–87. <https://doi.org/10.1016/j.jhydrol.2006.10.001>.
- Wang, L.u., Ai, T., Shen, Y., Li, J., 2020. The isotropic organization of DEM structure and extraction of valley lines using hexagonal grid. *Trans. GIS* 24 (2), 483–507. <https://doi.org/10.1111/tgis.12611>.
- White, D., Kimerling, A.J., Sahr, K., Song, L., 1998. Comparing area and shape distortion on polyhedral-based recursive partitions of the sphere. *Int. J. Geogr. Inf. Sci.* 12 (8), 805–827. <https://doi.org/10.1080/136588198241518>.
- Wolock, D.M., McCabe, G.J., 1995. Comparison of single and multiple flow direction algorithms for computing topographic parameters in TOPMODEL. *Water Resour. Res.* 31 (5), 1315–1324. <https://doi.org/10.1029/95WR00471>.
- Wright, J.W., 2017. Regular hierarchical surface models: a conceptual model of scale variation in a GIS and its application to hydrological geomorphometry, School of Surveying. University of Otago, Dunedin, Otago, New Zealand, p. 348.
- Wu, W., Fan, Y., Wang, Z., Liu, H., 2008. Assessing effects of digital elevation model resolutions on soil–landscape correlations in a hilly area. *Agric. Ecosyst. Environ.* 126 (3–4), 209–216. <https://doi.org/10.1016/j.agee.2008.01.026>.
- Zhang, B., Zerubia, J., Olivo-Marin, J.C., 2007. Gaussian approximations of fluorescence microscope point-spread function models. *Appl. Opt.* 46, 1819–1829. <https://doi.org/10.1364/AO.46.001819>.
- Zhao, G., Pang, B., Xu, Z., Peng, D., Xu, L., 2019. Assessment of urban flood susceptibility using semi-supervised machine learning model. *Sci. Total Environ.* 659, 940–949. <https://doi.org/10.1016/j.scitotenv.2018.12.217>.